



# Unsaturated single-atom CoN<sub>3</sub> sites for improved fenton-like reaction towards high-valent metal species

Junsheng Song<sup>a</sup>, Nannan Hou<sup>a,\*</sup>, Xiaocheng Liu<sup>a</sup>, Markus Antonietti<sup>b</sup>, Yang Wang<sup>b,\*</sup>, Yang Mu<sup>a,\*</sup>

<sup>a</sup> CAS Key Laboratory of Urban Pollutant Conversion, Department of Environmental Science and Engineering, University of Science and Technology of China, 230026 Hefei, China

<sup>b</sup> Department of Colloid Chemistry, Max Planck Institute of Colloids and Interfaces, 14476 Potsdam, Germany



## ARTICLE INFO

### Keywords:

Single-atom Co catalysts  
Unsaturated coordination regulation  
Peroxymonosulfate activation mechanism  
Formation of high-valent Co species

## ABSTRACT

High-valent metal species hold promise for selective removal of organic pollutants in wastewater, which necessitate two or more electrons transfer to allow intensive electron from catalysts to PMS. Herein, we design undercoordinated single-atom CoN<sub>3</sub> catalyst for boosted generation of high-valent Co species in peroxymonosulfate activation process, to be carefully distinguished from the traditional saturated CoN<sub>4</sub> configuration. Enabled by temperature-dependent magnetization measurements, in-situ Raman spectra and electrochemical tests, we found that the unsaturated Co sites in CoN<sub>3</sub> with higher spin state can afford enhanced electron-donating ability and intensive electron flow to drive the valence transformation from Co(II) to Co(IV), while the saturated ones in CoN<sub>4</sub> with lower spin state only trigger Co(II)/Co(III) conversion and subsequently produce free radicals. This work highlights the pivotal role of coordination environment for electron flow regulation in Fenton-like catalysts to alleviate water pollution dilemma and advance environmental remediation technologies.

## 1. Introduction

Peroxymonosulfate (PMS)-based advanced oxidation processes are central to water decontamination. Attempts to advance PMS activation efficiency have been exemplified by single atom catalysts (SACs) [1,2]. This is not only due to the utmost atom utilization and excellent catalytic performance but also the simplified structure that provides an ideal platform to explore the structure-activity relationship at the atomic level [3]. Typically, single metal atoms loaded in a nitrogen-doped carbon matrix (M-N-C) are quite competitive candidates, which can be obtained by simple pyrolysis of commercially available metal precursors with nitrogen and carbon sources [4]. Among them, cobalt (Co)- and iron (Fe)-based M-N-C configurations have been recognized as leading catalysts for PMS activation [5,6], with free radicals ( $\bullet\text{OH}/\text{SO}_4^\bullet$ ), singlet oxygen ( $^1\text{O}_2$ ) or high-valent metal species being reactive species to oxidize pollutants. It is worth reminding that the formation of specific reactive oxygen species (ROS) to allow improved catalytic performance is still highly desired.

Note that regulating the coordination environment of single atoms helps to tune the intrinsic performance in Fenton-like reactions [7].

Accordingly, the geometrical structure and electronic state of single atoms are tunable in response to coordination environment changes, which reshapes the absorption activity of the substrate towards metal sites and thus tailors the catalytic performance [8]. More importantly, the altered coordination environment is expected to affect PMS activation pathways by tailoring electron flow between PMS and single atoms to afford oriented generation of specific ROS. For instance, the CoN<sub>4</sub> configuration is identified as an efficient electron donor for PMS reduction to produce free radicals ( $\bullet\text{OH}/\text{SO}_4^\bullet$ ) [5]. However, when the Co atoms coordinate with N atoms to form two adjacent N-C fragment edges (denoted as CoN<sub>2+2</sub>), the lowered electropositivity of central Co atoms drives the electron flow from PMS to CoN<sub>2+2</sub> and triggers the selective formation of singlet oxygen ( $^1\text{O}_2$ ) [9]. Therefore, rational control of M-N-C configurations via coordination environment regulation to tailor electron flow between catalysts and PMS is promising to advance the intrinsic activity of PMS activation via radical or non-radical pathways.

Compared with free radicals and  $^1\text{O}_2$ , high-valent metal species are prized for their appreciable oxidizing strength while leaving the catalyst support unaffected [6]. However, the generation of either free radicals

\* Corresponding authors.

E-mail addresses: [hounan@ustc.edu.cn](mailto:hounan@ustc.edu.cn) (N. Hou), [Yang.Wang@mpikg.mpg.de](mailto:Yang.Wang@mpikg.mpg.de) (Y. Wang), [yangmu@ustc.edu.cn](mailto:yangmu@ustc.edu.cn) (Y. Mu).

or high-valent species requires PMS reduction by electron donation from SACs, making the specific strategy to selectively form high-valent metal species quite challenging. Fortunately, the formation of free radicals only requires one-electron transfer while the latter requires two or more and thus highlights the importance of intensive electron flow from catalysts to PMS [10–13]. Establishing unsaturated metal sites offers the possibility to address this issue. Firstly, unsaturated metal sites with lower coordination numbers are presented with more accessible d-orbitals and decreased steric hindrance [14], which are expected to promote interaction with reactants or converted intermediates during the PMS activation process. Secondly, the site-specific contributions from the unsaturated configuration are further emphasized here, as their lower thermodynamic stability can be related to a more negative electron work-function, which again increases the electron density in the Co centers [15,16]. Following these arguments, we propose that the development of unsaturated metal sites in the M-N-C configuration increases the availability of their electrons, which may trigger intensive electron flow to PMS to generate rather selectively the wanted high-valent metal species.

In this work, we successfully synthesized an unsaturated single-atom  $\text{CoN}_3$  catalyst as an example through rational regulation of pyrolysis conditions, which showed evidently boosted degradation rates of various organic pollutants compared to the traditional saturated  $\text{CoN}_4$  configuration. We found that unsaturated  $\text{CoN}_3$ , different from the reported  $\text{CoN}_4$  or  $\text{CoN}_{2+2}$ , could efficiently activate PMS to generate high-valent Co species (Co(IV)), which dominated the subsequent degradation of contaminants. Electrical tests and in-situ Raman measurements revealed that the formation of high-valent Co experienced a two-step oxidation process as  $\text{Co}(\text{II})/\text{Co}(\text{III})$  and subsequent  $\text{Co}(\text{III})/\text{Co}(\text{IV})$  transformation. The intrinsic driving force for Co(IV) conversion was primarily the intensive electron flow from the catalyst to PMS, which was a reflection of the enhanced electron-donating ability of unsaturated single Co atoms affording a higher spin state, and the one with lower spin states may only produce free radicals. Our findings unravel the formation mechanism of high-valent Co species and free radicals in PMS activation, upon which the rational design of tunable atomic active sites with both high reactivity and selectivity in Fenton-like reactions can be expected.

## 2. Experimental

### 2.1. Materials synthesis and characterization

The  $\text{CoN}_3$  and  $\text{CoN}_4$  catalysts in this work were fabricated by one-pot pyrolysis process using chitosan and cobalt salt as precursors (Text S1). The morphology and coordination structure of single atoms were mainly characterized by aberration-corrected high-angle annular dark-field-scan transmission electron microscopy (AC-HADD-STEM), soft and hard X-ray absorption spectroscopy (XAS). Materials characterizations in more details are provided in Text S2.

### 2.2. Measurements and analysis on catalytic performance

Rhodamine B (RhB), Orange II, bisphenol A (BPA), ciprofloxacin (CIP) and tetracycline (TTC) were selected as model pollutants to evaluate the catalytic performance of  $\text{CoN}_3$  and  $\text{CoN}_4$  in terms of pollutant removal upon PMS activation, and details are shown in Text S3. In addition, in situ Raman spectra were collected to measure the reactivity of PMS activation on the surface of single-atom catalysts (Text S4).

Electron spin resonance (EPR) was conducted to detect  $\bullet\text{OH}/\text{SO}_4^\bullet$  and  $^1\text{O}_2$  [9]. Methyl phenyl sulfoxide (PMSO) was used as a probe to explore the existence of high-valent Co species [17]. Quenching experiments with different quenching media were conducted to screen the primary reactive species in  $\text{CoN}_3$  and  $\text{CoN}_4$  systems (Text S5). Details of density functional theory (DFT) calculations are given in Text S6.

### 2.3. Electrical measurements

We performed open-circuit potential (OCP) tests and cyclic voltammetry (CV) measurements to evaluate the electron transfer between single-atom catalysts and PMS. These electrochemical tests were conducted in a customized three-electrode setup. A glassy carbon electrode loaded with single-atom catalysts, a platinum wire electrode and a Ag/AgCl electrode were used as the working electrode, counter electrode and reference electrode, respectively.  $\text{Co-N-C}$  catalysts (8 mg) and Nafion solution (5 wt%, 80  $\mu\text{L}$ ) were dispersed in a water/ethanol mixed solution (50:50, v/v, 1 mL) by ultrasonication for 20 min. Then, the mixture (3  $\mu\text{L}$ ) was dropped three times onto the surface of the polished glassy carbon electrode and dried at room temperature for 24 h. The scanning rate in CV tests was 200 mV/s.

## 3. Results and discussion

### 3.1. Characterizations of $\text{CoN}_4$ and $\text{CoN}_3$ catalyst

The synthetic procedures of traditional  $\text{CoN}_4$  and unsaturated  $\text{CoN}_3$  catalysts are briefly depicted in Fig. 1a. Here, the earth-abundant polymer chitosan was selected as a natural chelating substrate due to its rich amino groups that showed strong affinity to transition metal cations. [18] By calcining the mixture of chitosan and cobalt salts through one-pot pyrolysis process, it is promising to synthesize single-atom Co materials. The thermogravimetric curve of the mixed precursors (Fig. S1a) suggested that the mixture was stabilized in mass above 500 °C (i.e., the deriv. weight turned to be a constant above 500 °C). When temperature was lower than 500 °C, it was assumed that the mixture experienced an evident weight-loss process dominated by dehydration and dehydroxylation, which lead to the weight loss instability, suggesting it was unfavorable for the formation of structurally stable materials below 500 °C. Therefore, a series of Co, N-doped carbon materials (denoted as Co/NC) were synthesized above 500 °C. The XRD patterns of Co/NC-500 and Co/NC-600 (Figs. S1b) indicated the absence of peaks assigned to metallic Co or Co compounds, signifying highly dispersed Co species within the catalysts. However, when the pyrolysis temperature was higher than 600 °C, both Co/NC-620 and Co/NC-650 (Fig. 1b) showed characteristic peaks of metallic Co, suggesting that temperatures above 600 °C was not conducive to the synthesis of stable single-atom materials. Following these facts, two catalysts denoted as Co/NC-500 and Co/NC-600 were synthesized, which were later determined to be single-atom catalysts  $\text{CoN}_4$  and  $\text{CoN}_3$ , respectively. The coordination environment of single atoms could be readily tunable by changing the pyrolysis temperature, as a higher temperature would contribute to a more evident release of N-containing elements and therefore benefit the formation of unsaturated  $\text{CoN}_3$  at 600 °C. [19] The Co contents of  $\text{CoN}_4$  and  $\text{CoN}_3$  were determined to be 2.8 wt% and 2.9 wt% via inductively coupled plasma optical emission spectroscopy (ICP-MS), respectively (Table S2). In addition,  $\text{CoN}_3$  was characterized by improved water dispersibility from pH of 4.7–11.0, as deduced from zeta potential measurements (Fig. S2).

To demonstrate the atomic dispersion of Co atoms in both  $\text{CoN}_3$  and  $\text{CoN}_4$ , multiform TEM images and extended X-ray absorption fine structure (EXAFS) spectra were recorded. TEM images (Fig. S3) further excluded the formation of aggregated Co species in  $\text{CoN}_4$  and  $\text{CoN}_3$ , keeping good consistency with the XRD results (Fig. S1). HAADF-STEM images and energy-dispersive X-ray (EDX) element mapping images were indicative of a homogenous distribution of Co species (Fig. 1b). Then, AC-HADD-STEM images (Fig. 1c, Fig. 1d) and EXAFS (Fig. 2b) spectra were recorded to verify the atomic dispersion of Co in the two samples. Evidently, single Co atoms without aggregation could be directly observed, which were marked as isolated bright dots in  $\text{CoN}_3$  and  $\text{CoN}_4$ . In addition, the EXAFS spectra point to the absence of Co-Co bonds in R space, further verifying the atomic dispersion of Co atoms. The combined results confirmed the formation of single Co atoms in

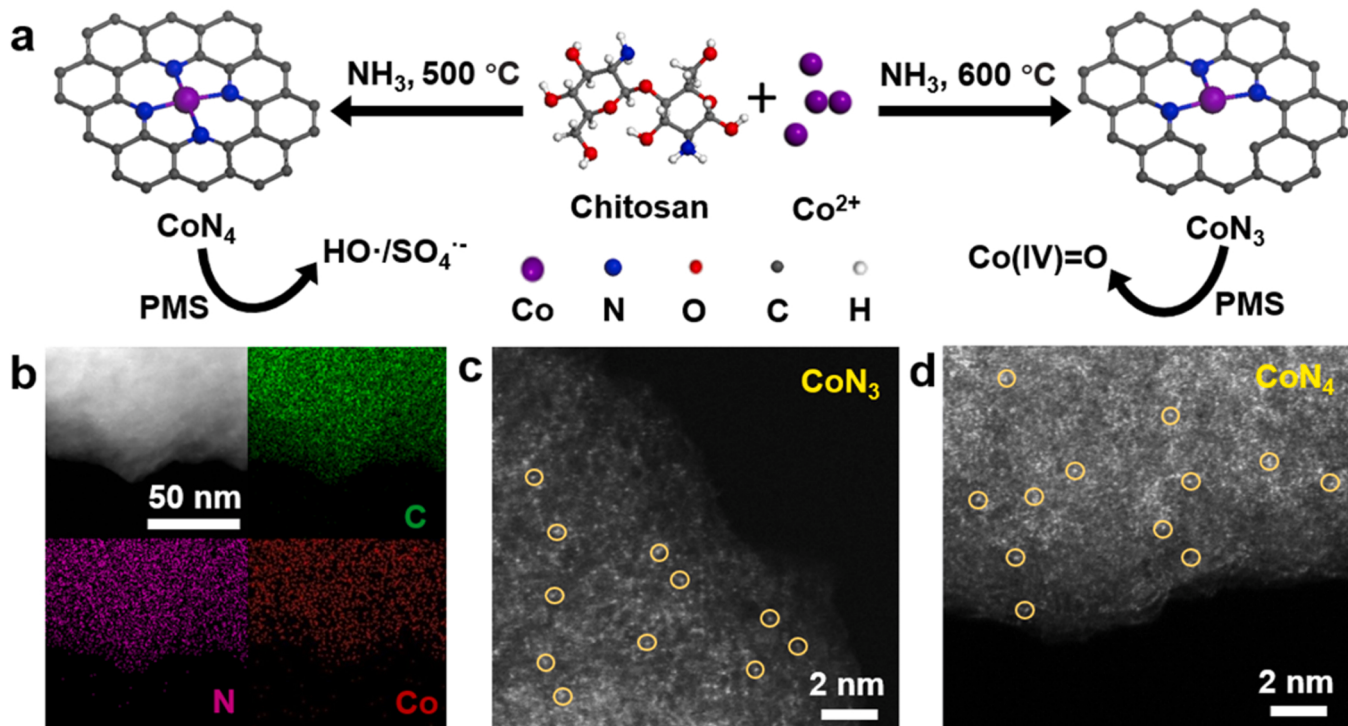


**Fig. 1.** (a) Formation processes of  $\text{CoN}_4$  and  $\text{CoN}_3$ . (b) STEM image and the corresponding EDX mapping results of  $\text{CoN}_3$ . (c, d) AC-HAADF-STEM images of (c)  $\text{CoN}_3$  and (d)  $\text{CoN}_4$ .

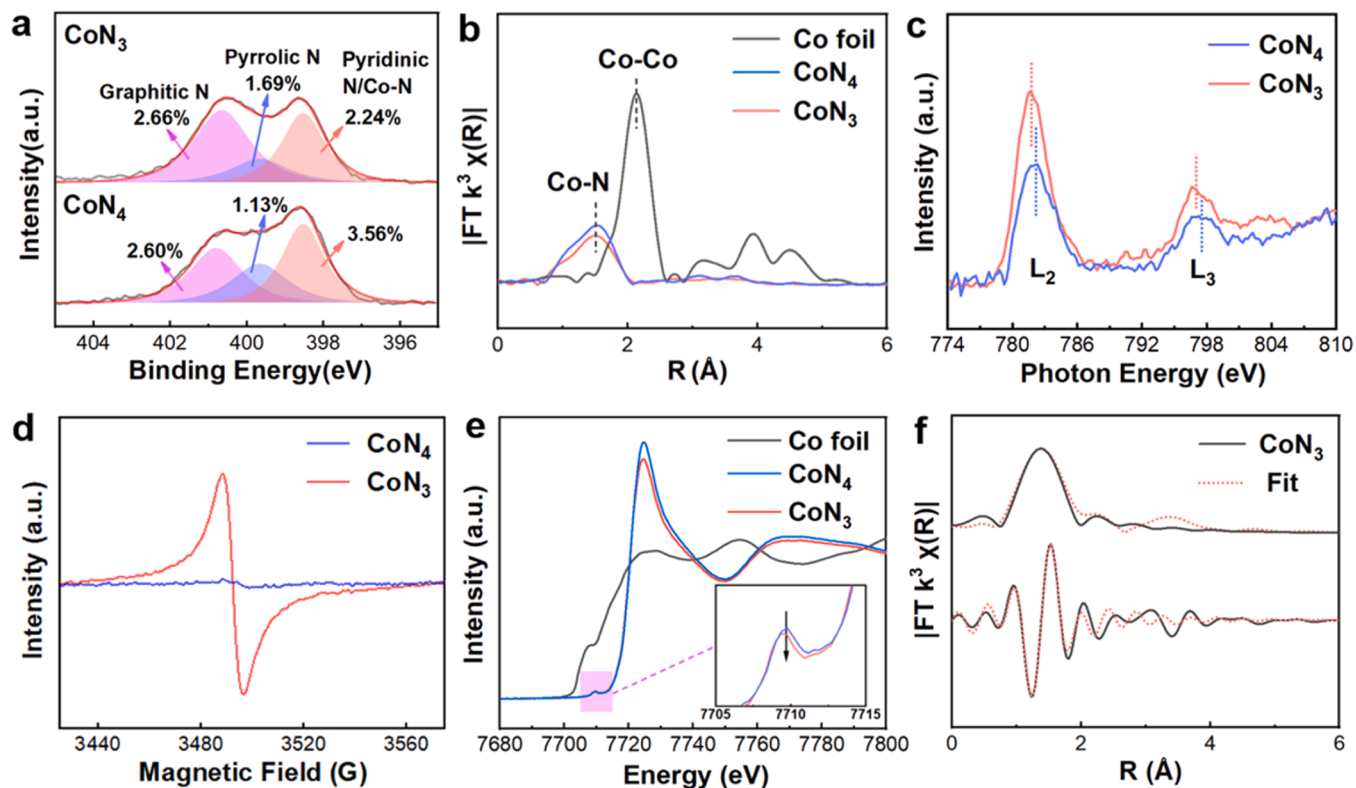


**Fig. 2.** (a) N 1 s XPS spectra and (b) FT-EXAFS spectra of  $\text{CoN}_3$  and  $\text{CoN}_4$ . (c) Co L-edge XANES spectra, (d) EPR spectra and (e) Co K-edge XANES spectra of  $\text{CoN}_3$  and  $\text{CoN}_4$ . (f) Corresponding EXAFS fitting curves for  $\text{CoN}_3$ .

$\text{CoN}_4$  and  $\text{CoN}_3$ .

To further explore the electronic structures and coordination environments of single Co atoms in  $\text{CoN}_4$  and  $\text{CoN}_3$ , X-ray photoelectron

spectroscopy (XPS) and soft and hard XAS were employed. In the C K-edge spectra of  $\text{CoN}_3$  and  $\text{CoN}_4$  (Fig. S4), the peak centered at 288.4 eV indicated the formation of  $\sigma^*$  (C-N-Co) bonds. [20] The peaks of the N

K-edge spectra (Fig. S5a) centered at 397.8, 400.5, and 406.0 eV revealed the existence of  $\sigma^*$  (pyridinic N),  $\sigma^*$  (pyrrolic N) and  $\pi^*$  (graphitic N), respectively. [20] The new peak at 399.1 eV suggested that Co atoms were coordinated with pyridinic N atoms. [21] The XPS N 1 s spectra of both CoN<sub>4</sub> and CoN<sub>3</sub> could be deconvoluted into three peaks (Fig. 2a), which were assigned to graphitic N (401.1 eV), pyrrolic N (399.6 eV) and pyridinic N (398.5 eV). [22] The position of pyridinic N was obviously shifted compared to NC-500 and NC-600, while the position of graphitic N and pyrrolic N remained unchanged (Fig. S5b), also suggesting that Co was coordinated with pyridinic N, [23] in line with the N K-edge spectra (Fig. S5a). Specifically, the N content in CoN<sub>3</sub> annealed under higher temperature (600 °C) was determined to be lower than that in CoN<sub>4</sub> (6.6 wt% vs 7.9 wt%) (Table S1). It was noted that a higher annealing temperature (600 °C) resulted in a lower proportion of pyridinic N/Co-N in CoN<sub>3</sub> (2.24 wt% vs 3.56 wt% in CoN<sub>4</sub>), suggesting the altered coordination of pyridinic N atoms around central Co. Compared those values with the determined Co content by ICP, it became clear that the pyridinic N atoms in CoN<sub>3</sub> were not sufficient to realize a fourfold coordination around the central Co. This was supported by the attenuated intensity of the Co-N peak in the EXAFS spectra of CoN<sub>3</sub> (Fig. 2b), which underlined a decreased coordination number of N. Second, the Co L-edge XANES and EPR spectra indicated increased nitrogen vacancies (NVs) in CoN<sub>3</sub> compared to CoN<sub>4</sub>. Negative shifts of the L<sub>3</sub> (779.6 eV) and L<sub>2</sub> (776.4 eV) peaks in the Co L-edge XANES spectra were observed in CoN<sub>3</sub> (Fig. 2c), quantifying the electrochemically negative ("less binding") shift of the local electron density. [24] The increased NVs in CoN<sub>3</sub> were beneficial for promoting the access to the accessible electrons of the Co centers. In addition, the EPR signal arising from the electrons trapped in NVs was dramatically strengthened in CoN<sub>3</sub> (Fig. 2d), matching well with the XANES (Co L-edge) results.

[25] Third, XANES of Co K-edge spectra (Fig. 2e) revealed the similar valence state of CoN<sub>3</sub> and CoN<sub>4</sub>, which was close to + 2, as revealed by the XPS data (Fig. S6). Additionally, the decreased intensity of pre-edge peak of CoN<sub>3</sub> suggested reduced symmetry (Fig. 2e). [26] Having ascertained the lowered Co-N coordination to the support, increased NVs and lowered symmetry of CoN<sub>3</sub> relative to CoN<sub>4</sub>, we simulated the EXAFS (Fig. 2f, Fig. S7 and Table S2) spectra of CoN<sub>3</sub> and CoN<sub>4</sub>, which matched well with the experimental results. The Co coordination numbers in CoN<sub>3</sub> and CoN<sub>4</sub> were determined to be 3.3 and 3.8 based on our fitting results, respectively. We also synthesized Co/NC-550 catalyst calcined at 550 °C, the coordination number of which was determined to be 3.6 (Fig. S8, Table S3). Note that the Co coordination numbers of Co/NC-500 and Co/NC-550 were 3.8 and 3.6, respectively. It is therefore reasonable using CoN<sub>4</sub> model to fit the actual structure of Co/NC-500, relative to Co/NC-550. Meanwhile, CoN<sub>3</sub> configuration fits properly for Co/NC-600. Through DFT calculations, the estimated binding energy of CoN<sub>4</sub> and CoN<sub>3</sub> was - 6.9 eV and - 5.6 eV, respectively, indicating the favorable thermodynamic structural stability of the two configurations [27]. Collectively, the successful preparation of traditional CoN<sub>4</sub> and unsaturated CoN<sub>3</sub> SACs was validated.

### 3.2. Enhanced generation of high-valent Co species for CoN<sub>3</sub> compared to CoN<sub>4</sub>

RhB was initially selected as a model compound to evaluate the degradation efficiency of CoN<sub>3</sub> and CoN<sub>4</sub> via PMS activation. Compared to the low removal efficiency of less than 40% within 5 min in the CoN<sub>4</sub>/PMS system, RhB was completely removed in CoN<sub>3</sub>/PMS within 5 min with a  $k$  (pseudo-first-order kinetic constant) value of 1.1 min<sup>-1</sup> at pH 7.0, which was 11.8 times higher than that of CoN<sub>4</sub> (Fig. 3a, Figs. S9-

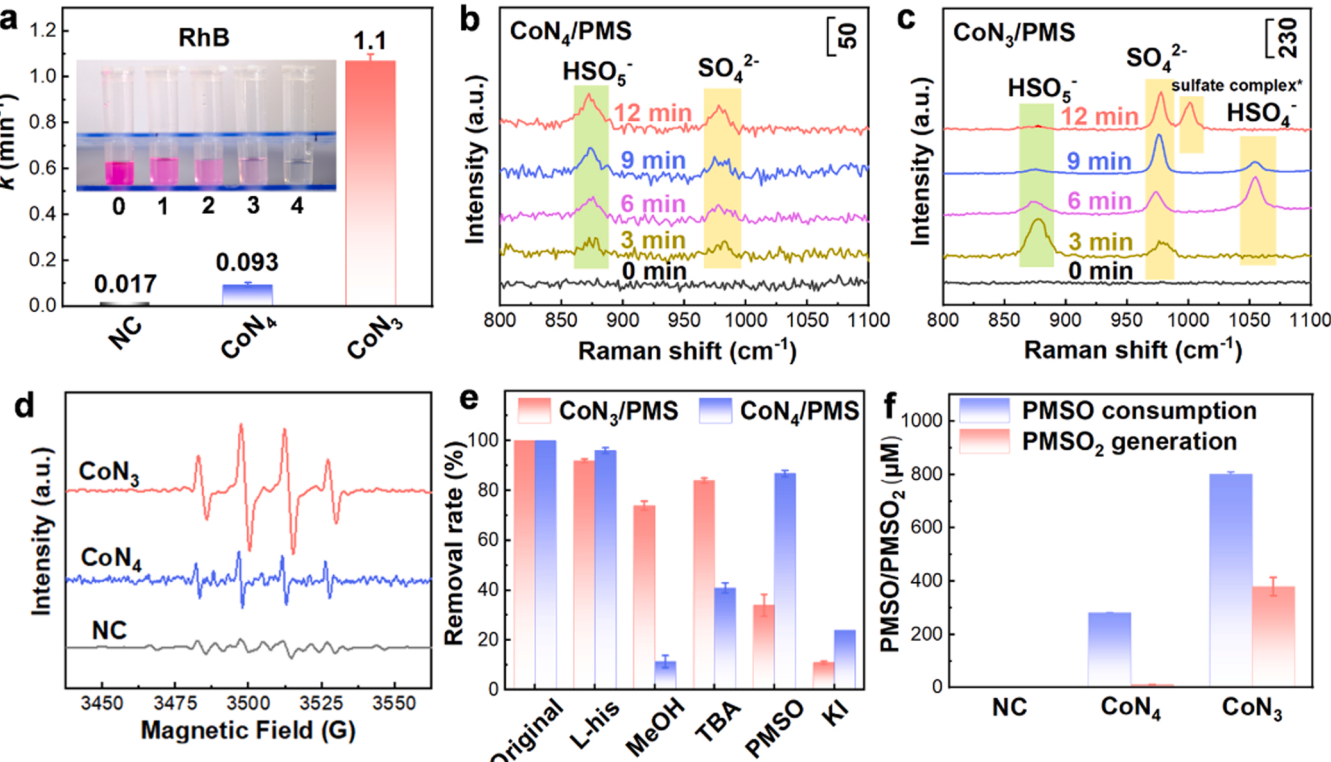


**Fig. 3.** (a) RhB degradation rate constant of CoN<sub>3</sub>, CoN<sub>4</sub> and NC, inset: the color change of RhB at different reaction times (min). Reaction conditions: catalyst dosage = 0.1 g/L, [PMS]<sub>0</sub> = 0.8 mM, [RhB]<sub>0</sub> = 45  $\mu$ M, pH<sub>0</sub> = 7.0. These conditions were generally applicable if not otherwise specified. (b,c) In situ Raman spectra of (b) CoN<sub>4</sub>/PMS and (c) CoN<sub>3</sub>/PMS. The labels in the upper-right corners of (b,c) are the scale bars of the vertical axis. (d) EPR spectra of CoN<sub>4</sub>-, CoN<sub>3</sub>- and NC-catalyzed PMS activation systems (using DMPO as a probe). (e) Comparison of the removal efficiency in two systems under different quenching conditions, [L-his] = 10 mM, [TBA] = [MeOH] = 0.5 M, [PMSO] = 15 mM, [KI] = 0.04 M (if needed), (f) PMSO consumption and PMSO<sub>2</sub> generation in different catalytic systems, [PMSO]<sub>0</sub> = 2 mM.

**S10**). TOC removal of RhB reached 56.7% within 90 min in  $\text{CoN}_3/\text{PMS}$ , significantly higher than that of  $\text{CoN}_4$  (33.5%) (Fig. S11). Moreover,  $\text{CoN}_3$  retained good activity over the first three cycles. Even in the fourth run, the degradation rate maintained high up to 70% (Fig. S12). Meanwhile, the peak positions of Co 2p spectra of  $\text{CoN}_3$  after use highly resembled that of the fresh one, suggesting its favorable structural stability (Fig. S13). The  $\text{CoN}_3/\text{PMS}$  system also showed excellent RhB decomposition performance within a wide pH range from 3.0 to 11.0 (Fig. S14). Additionally, neither the anions ( $\text{Cl}^-$ ,  $\text{HCO}_3^-$ , and  $\text{SO}_3^{2-}$ ) nor the cations ( $\text{Na}^+$ ,  $\text{K}^+$  and  $\text{Ca}^{2+}$ ) significantly influence the degradation rate of RhB (Fig. S15), indicating that the  $\text{CoN}_3/\text{PMS}$  system is less likely to be affected by different water constituents. Furthermore, the  $\text{CoN}_3/\text{PMS}$  system was able to effectively remove various organic pollutants including Orange II, BPA, CIP and TTC (Fig. S16), suggesting its good practicability.

To intuitively monitor the surface reactivity of single-atom Co sites during the PMS activation process, *in situ* Raman spectra were collected in both  $\text{CoN}_3/\text{PMS}$  and  $\text{CoN}_4/\text{PMS}$  systems. The peak centered at  $881\text{ cm}^{-1}$  was assigned to the adsorbed PMS ( $\text{HSO}_5^-$ ), while peaks at  $978$  and  $1060\text{ cm}^{-1}$  were associated with  $\text{SO}_4^{2-}$  and  $\text{HSO}_4^-$ , two products after PMS activation. [28] As depicted in Fig. 3b,  $\text{HSO}_5^-$  on the surface of  $\text{CoN}_4$  was slowly adsorbed and accumulated, accompanied by its partial conversion to produce  $\text{SO}_4^{2-}$ . Comparatively, the rapid consumption of PMS coupled with the immediate appearance of  $\text{SO}_4^{2-}$  and  $\text{HSO}_4^-$  signified the much higher reactivity of  $\text{CoN}_3$  towards PMS activation (Fig. 3c).  $\text{HSO}_4^-$  was further transformed into  $\text{H}^+$  and  $\text{SO}_4^{2-}$  with prolonged reaction time. Interestingly, a new peak at  $1003\text{ cm}^{-1}$  was detected, which might be attributed the surface-bound sulfate complex [29], suggesting the rapid PMS activation process. The consumption rate of PMS was up to 58% in  $\text{CoN}_3/\text{PMS}$  within 12 min, which only accounted for 20% in the  $\text{CoN}_4/\text{PMS}$  system (Fig. S17), indicating that  $\text{CoN}_3$  significantly facilitated the consumption and activation of PMS, keeping good consistency with Raman results.

Such a high catalytic activity of  $\text{CoN}_3$  raised our concern to determine the leading reactive species. EPR was conducted to semi-quantitatively explore the concentration of reactive oxygen species ( $\bullet\text{OH}/\text{SO}_4^\bullet$  and  ${}^1\text{O}_2$ ), which have been widely reported in single-atom Co catalyzed PMS activation processes. [30–32] As depicted in Fig. 3d, both  $\bullet\text{OH}$  and  $\text{SO}_4^\bullet$  were generated in both  $\text{CoN}_4$  and  $\text{CoN}_3$ , while the signal intensity of  $\bullet\text{OH}$  in the  $\text{CoN}_3$  system was evidently higher than that in the  $\text{CoN}_4$  system. This was also supported by the benzoic acid (BA) probe experiments, which specifically converted to *p*-HBA (*p*-hydroxybenzoic acid) when reacting with  $\bullet\text{OH}$  [33]. The accumulated concentration of *p*-HBA within 5 min in the  $\text{CoN}_3$  system was two times higher than that of  $\text{CoN}_4$  (Fig. S18), further indicating the generation of more  $\bullet\text{OH}$  in  $\text{CoN}_3/\text{PMS}$ . On the other hand, the intensity of the triplet signals of  $\text{TEMPO}^\bullet\text{O}_2$  in both systems was in close proximity to the background of TEMP (Fig. S19), suggesting negligible  ${}^1\text{O}_2$  formation in the two systems.

Next, we carried out quenching experiments with different quenching media to differentiate the contributions of free radicals in the two systems. The results showed that  ${}^1\text{O}_2$  (quenching agent: L-histidine) was not the main contributor to the degradation of RhB in both  $\text{CoN}_3/\text{PMS}$  and  $\text{CoN}_4/\text{PMS}$  systems (Fig. 3e) [34]. In the  $\text{CoN}_4/\text{PMS}$  system, the degradation efficiency was significantly lowered when methanol (radical scavenger for  $\text{SO}_4^\bullet$  and  $\bullet\text{OH}$ ) was added, indicating the major contribution of free radicals in  $\text{CoN}_4$  [35]. The increased concentration of free radicals in the  $\text{CoN}_3/\text{PMS}$  system, however, did not constitute the dominant role in  $\text{CoN}_3/\text{PMS}$ , as evidenced by the slightly decreased removal efficiency using methanol or TBA (radical scavenger for  $\bullet\text{OH}$ ) as quenching reagent (Fig. 3e, Fig. S20). We further used methyl phenyl sulfone (PMSO) to detect the possible existence of high-valent Co species reported in homogenous  $\text{Co}^{2+}$  or heterogenous  $\text{CoCO}_3$ -catalyzed PMS activation processes. [17,36,37] The ratio of  $\Delta\text{PMSO}_2/\Delta\text{PMSO}$  can be used to semi-quantify the content of high-valent Co species, as PMSO could be selectively oxidized to  $\text{PMSO}_2$ , different from free radicals

mediated pathways [17]. As such,  $\Delta\text{PMSO}_2/\Delta\text{PMSO}$  reached to 52% in the  $\text{CoN}_3/\text{PMS}$  system. However,  $\Delta\text{PMSO}_2/\Delta\text{PMSO}$  was only 9% in the  $\text{CoN}_4/\text{PMS}$  system, indicating that  $\text{CoN}_3/\text{PMS}$  significantly facilitated the generation of high-valent Co species. (Fig. 3f, Figs. S21 and S22) than in  $\text{CoN}_4$ , demonstrating that  $\text{CoN}_3$  significantly promoted the generation of high-valent Co species. To clarify the contributions of high-valent Co species towards pollutant removal, PMSO was also used as a quenching agent (Fig. 3e) [38]. As a result, the removal rate was only slightly decreased in  $\text{CoN}_4/\text{PMS}$  with the addition of PMSO, which was substantially reduced when PMSO was added into  $\text{CoN}_3/\text{PMS}$ , highlighting the leading role of high-valent Co species. Moreover, KI (scavenger for surface reactions) significantly inhibited the degradation efficiency in two systems [39], elucidating the primary contributions from surface-bound high-valent Co species in  $\text{CoN}_3/\text{PMS}$  and surface radicals in  $\text{CoN}_4/\text{PMS}$ . Collectively, these results clearly demonstrated that the unsaturated single-atom  $\text{CoN}_3$  markedly enhanced the intrinsic activity of PMS activation reactions towards pollutant removal via rather selective generation of high-valent Co species.

### 3.3. Mechanism study in the conversion of high-valent Co species

DFT was used to reveal the enhanced affinity and electron transfer between unsaturated  $\text{CoN}_3$  and PMS. Specifically, the adsorption energy of PMS towards coordination-saturated models was calculated to be  $1.85$ ,  $-2.00$ ,  $-2.16$ ,  $-1.99$ ,  $-2.07$  and  $-1.65\text{ eV}$  for  $\text{CoN}_4$ ,  $\text{CoN}_3\text{C}_1$ ,  $\text{CoN}_3$  (without N vacancies), [40]  $\text{CoN}_2\text{C}_2^a$ ,  $\text{CoN}_2\text{C}_2^b$  and  $\text{CoN}_1\text{C}_3$ , respectively. However, it turned out to be much lower for unsaturated  $\text{CoN}_3$  ( $-2.50\text{ eV}$ ) (Fig. 4a, Fig. S23), suggesting better affinity of  $\text{CoN}_3$  to PMS. In terms of the electronic state, the single Co atoms in  $\text{CoN}_3$  showed a d-band center of  $-0.49\text{ eV}$ , much higher than that in  $\text{CoN}_4$  ( $-2.17\text{ eV}$ ) (Fig. 4b), also indicating the enhanced adsorption ability [41]. In addition, it is worth noting that the electrons of the Co 3d orbital in  $\text{CoN}_3$  were more evidently overlapped with the absorbed O 2p in PMS near the Fermi level compared to  $\text{CoN}_4$  (Fig. 4b), indicating a stronger interaction and easier electron transfer between  $\text{CoN}_3$  and PMS. This might stem from the difference in the electron-donating ability of two different single-atom configurations, which was related to the arrangement of the d-orbital electrons. The d-orbitals might split into higher energy level groups and lower ones under the influence of the ligand. If the d-electrons were to be filled in higher energy level orbitals, they were more active and easily lost. Then, the single atoms appeared to be situated in high spin state [42]. Temperature-dependent magnetization tests at  $H = 300\text{ Oe}$  were performed to evaluate the difference in spin state between  $\text{CoN}_4$  and  $\text{CoN}_3$  [43]. Considering that the order of the spin state is positively correlated with the effective magnetic moment ( $\mu_{\text{eff}}$ ) value, which is consistent with the Curie constant ( $C$ ,  $\mu_{\text{eff}} = (8\text{ C})^{0.5}\mu_B$ , and  $\mu_B$  is Bohr magneton), we calculated the  $C$  value through the linear fitting of the  $\chi^{-1}\text{-T}$  curve based on Curie-Weiss law ( $\chi = C/(T - Q)$ ) (Fig. 4c). [44] As a result, the single Co atoms in the  $\text{CoN}_3$  configuration possessed a higher spin state with a higher  $\mu_{\text{eff}}$  value, suggesting its enhanced electron-donating ability induced by the unsaturated coordination environment (Fig. S24). It was proposed that the single Co atoms in the  $\text{CoN}_3$  moieties were less affected by the ligand compared to that in the  $\text{CoN}_4$  due to the partial absence of N ligand, which led to a decreased orbital splitting energy. Accordingly, the d-electrons were more prone to occupy the higher energy levels and thus trigger a higher spin state [45].

Following a theoretically modeled PMS reaction on  $\text{CoN}_3$  and  $\text{CoN}_4$  surfaces, we further uncovered that the electron transfer from  $\text{CoN}_3$  to PMS was stronger than that of  $\text{CoN}_4/\text{PMS}$  (Fig. 4d), as revealed by the higher Hirshfeld charge of central Co in  $\text{CoN}_3$  ( $|1.8\text{ e}|$  vs  $|1.4\text{ e}|$  in  $\text{CoN}_4$ ) [46]. The boosted electron transfer could also be reflected by electrochemical experiments. In the OCP tests (Fig. 4e), the increased OCP in the two systems was observed after adding PMS deduced electron transfer from single Co sites to PMS. Additionally, the larger potential gap in  $\text{CoN}_3/\text{PMS}$  suggested greatly enhanced electron transfer. In the

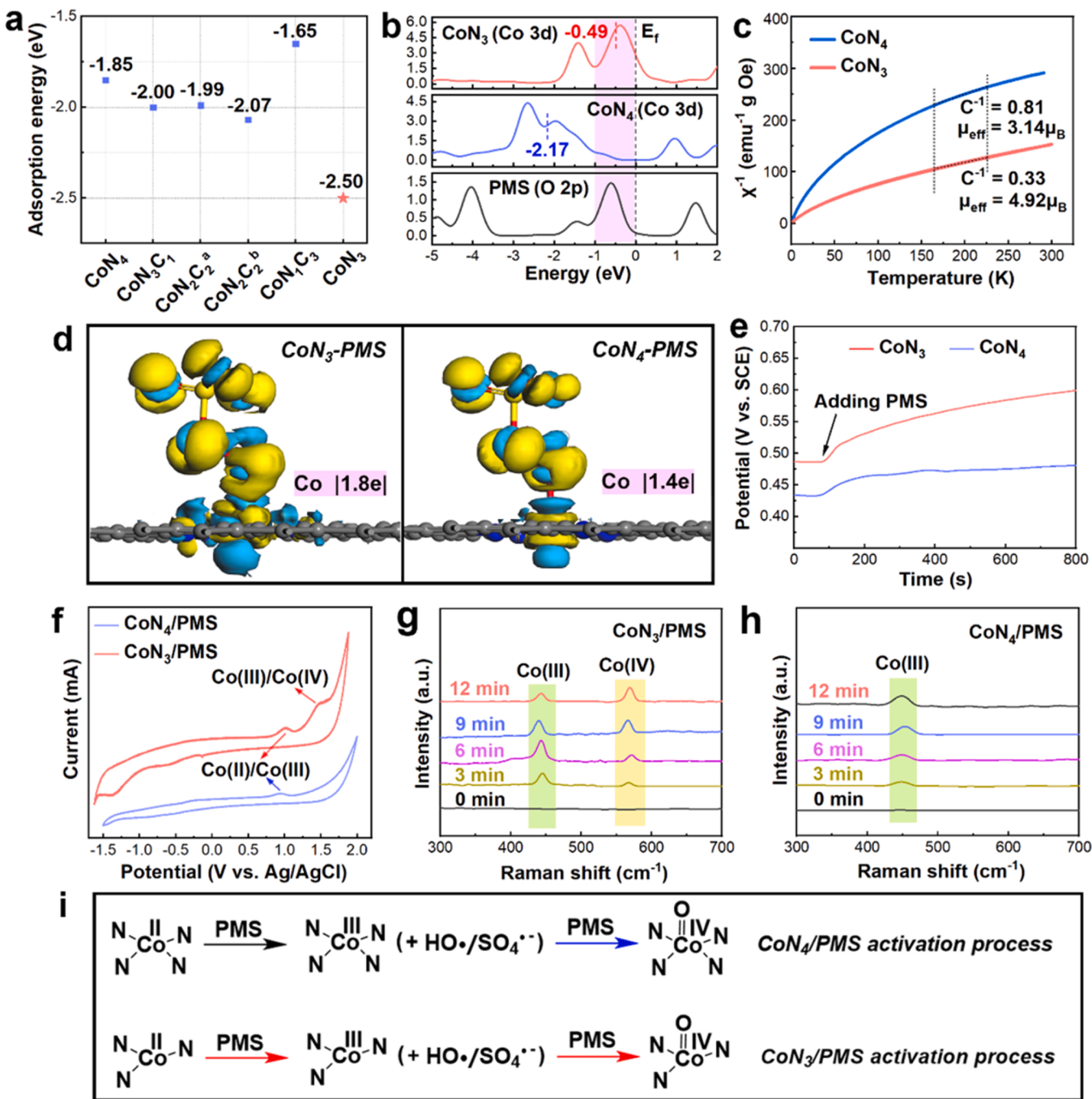


**Fig. 4.** (a) Adsorption energy profiles of PMS towards different Co-N-C configuration models. (b) Partial density of states of Co 3d in  $\text{CoN}_3$ , Co 3d in  $\text{CoN}_4$  and adsorbed O 2p in PMS. (c) Temperature-dependent inverse susceptibilities over  $\text{CoN}_3$  and  $\text{CoN}_4$  (C refers to Curie constant). (d) Electron density difference maps of  $\text{CoN}_3$ -PMS (left) and  $\text{CoN}_4$ -PMS (right), the light blue and yellow colors represent the electron depletion and electron accumulation, respectively. The exposed black and dark blue balls represent C and N atoms, while the Co atoms are wrapped in electron clouds. (e) OCP curves of  $\text{CoN}_3$  and  $\text{CoN}_4$ . PMS (2 mM) was added at 80 s (f) CV curves of  $\text{CoN}_4$  and  $\text{CoN}_3$ . In-situ Raman spectra of (g)  $\text{CoN}_3$ -PMS and (h)  $\text{CoN}_4$ -PMS under a 633 nm laser. (i) Proposed activation pathways of PMS catalyzed by  $\text{CoN}_4$  and  $\text{CoN}_3$ .

CV curves (Fig. 4f, Figs. S24 and S25), the peak at 1.1–1.2 V in both systems signified the Co(II)/Co(III) oxidation process. Impressively, a distinct peak at 1.4–1.5 V arising from the Co(III)/Co(IV) oxidation process was only detected in  $\text{CoN}_3$ -PMS [47]. The transformation of Co (III)/Co(IV) was also reflected by Raman signal. As shown in Fig. 4g and 4h, the peak located at 442 cm<sup>-1</sup> attributed to Co(III) was accumulated in the first 6 min and then weakened, while a signal assigned to Co(IV) at 572 cm<sup>-1</sup> gradually increased (Fig. 4f), suggesting the conversion of Co (III) to Co(IV) in  $\text{CoN}_3$ -PMS [48]. By contrast, the signal assigned to Co

(IV) was not detectable in  $\text{CoN}_4$ -PMS (Fig. 4g), collectively demonstrating the boosted conversion to high-valent Co(IV) via enhanced electron flow from  $\text{CoN}_3$  to PMS, in line with the results of CV tests. To sum up, the calculation of adsorption energy and spin state analysis suggested that  $\text{CoN}_3$  possessed better affinity with PMS and stronger electron-donating ability. As a result, more intensive electron flow from unsaturated Co sites to PMS was initiated, as revealed by electron density difference analysis and electrochemical measurements. Accordingly, the CV tests and in-situ Raman analysis collectively demonstrated

that  $\text{CoN}_3/\text{PMS}$  facilitated the generation of high-valent Co species.

Taking together, we rationally proposed the mechanism of PMS activation in two systems (Fig. 4f, Fig. S26). In  $\text{CoN}_4/\text{PMS}$ , the transformation of Co(II) to Co(III) occurred, accompanied by the activation of PMS to generate  $\bullet\text{OH}/\text{SO}_4^{\cdot+}$ . In  $\text{CoN}_3/\text{PMS}$ , the enhanced electron flow induced by the unsaturated coordination environment first enabled the valence shift from Co(II) to Co(III) and the generation of radicals and subsequently drove the transformation from Co(III) to Co(IV). Consequently, Co(IV) served as a strong oxidizer to destroy the electron-donating pollutant molecules and thus contributed to high degradation performance. Notably, Co(IV) might be reduced into Co(II) after reacting with pollutants (Figure S27), inducing a promoted catalytic cycle for an efficient PMS activation process.

#### 4. Conclusions

In summary, our experiments and theoretical analyses clearly demonstrated that unsaturated  $\text{CoN}_3$  dramatically enhanced the intrinsic activity of PMS activation. Compared to saturated  $\text{CoN}_4$ , which catalyzed PMS to generate free radicals with weak electron flow, the intensive electron flow from the catalyst to PMS promoted the formation of high-valent Co species by establishing unsaturated metal sites ( $\text{CoN}_3$ ) at the atomic level. This work highlights the importance of electron-flow regulation in PMS activation for the selective formation of reactive species, upon which the rational design of efficient catalysts for Fenton-like reactions can be achieved via microenvironment tailoring of single atoms.

#### CRediT authorship contribution statement

N.N.H., Y.W. and Y.M. designed and supervised the project. J.S.S. conducted the project. X.C.L. helped with the catalytic experiment. M.A. contributed to the analysis of synthesized materials and mechanism study. J.S.S., N.N.H., M.A., Y.W. and Y.M. wrote and revised the manuscript, and all the authors discussed the results and commented on the manuscript.

#### Declaration of Competing Interest

The authors declare that they have no known competing financial interests or personal relationships that could have appeared to influence the work reported in this paper.

#### Data Availability

Data will be made available on request.

#### Acknowledgement

We acknowledge the financial support from the National Natural Science Foundation of China (52200073, 52025101, U19A20108 and 51821006). Dr. Yang Wang thanks the Alexander von Humboldt Foundation for a postdoctoral fellowship. We thank the National Synchrotron Radiation Laboratory (NSRL, Hefei, China) for the help with the Soft XAS tests. The Supercomputing Center of USTC is acknowledged for the computational support.

#### Appendix A. Supplementary material

Materials synthesis and characterizations, details of catalytic performance measurements and reactive species clarification (Texts S1-S8); Zeta potential, XRD, XPS, K-edge XANES spectra, OCP analysis, pollutant removal, cyclic performance and computational models (Figures S1-S26); element content analysis and XAFS fitting parameters (Tables S1-S3).

#### Appendix A. Supporting information

Supplementary data associated with this article can be found in the online version at doi:10.1016/j.apcatb.2023.122368.

#### References

- [1] Y. Shang, X. Xu, B. Gao, S. Wang, X. Duan, Single-atom catalysis in advanced oxidation processes for environmental remediation, *Chem. Soc. Rev.* 50 (8) (2021) 5281–5322.
- [2] Y. Gao, T. W, C. Yang, C. Ma, Z. Zhao, Z. Wu, S. Cao, W. Geng, Y. Wang, Y. Yao, Y. Zhang, C. Cheng, Activity trends and mechanisms in peroxyomonosulfate-assisted catalytic production of singlet oxygen over atomic metal-N-C catalysts, *Angew. Chem. Int. Ed.* 60 (2021) 22513–22521.
- [3] Y. Luo, S. Zhang, H. Pan, S. Xiao, Z. Guo, L. Tang, U. Khan, B.F. Ding, M. Li, Z. Cai, Y. Zhao, W. Lv, Q. Feng, X. Zou, J. Lin, H.M. Cheng, B. Liu, Unsaturated single atoms on monolayer transition metal dichalcogenides for ultrafast hydrogen evolution, *ACS Nano* 14 (1) (2020) 767–776.
- [4] W. Liu, L. Zhang, X. Liu, X. Liu, X. Yang, S. Miao, W. Wang, A. Wang, T. Zhang, Discriminating catalytically active fenx species of atomically dispersed Fe–N–C catalyst for selective oxidation of the C–H bond, *J. Am. Chem. Soc.* 139 (2017) 10790–10798.
- [5] C. Chu, J. Yang, X. Zhou, D. Huang, J.H. Kim, Cobalt single atoms on tetrapyrromacrocyclic support for efficient peroxyomonosulfate activation, *Environ. Sci. Technol.* 55 (2) (2021) 1242–1250.
- [6] K. Qian, H. Chen, W. Li, Z. Ao, X. Guan, Single-atom Fe catalyst outperforms its homogeneous counterpart for activating peroxyomonosulfate to achieve effective degradation of organic contaminants, *Environ. Sci. Technol.* 55 (10) (2021) 7034–7043.
- [7] L. Jiao, W. Xu, Y. Zhang, Y. Wu, W. Gu, X. Ge, B. Chen, C. Zhu, S. Guo, Boron-doped Fe–N–C single-atom nanomolecules specifically boost peroxidase-like activity, *Nano Today* 35 (2020), 100971.
- [8] X. Li, H. Rong, J. Zhang, D. Wang, Y. Li, Modulating the local coordination environment of single-atom catalysts for enhanced catalytic performance, *Nano Res.* 13 (7) (2020) 1842–1855.
- [9] X. Mi, P. Wang, S. Xu, L. Su, H. Zhong, H. Wang, Y. Li, S. Zhan, Almost 100% peroxyomonosulfate conversion to singlet oxygen on single atom  $\text{CoN}_{2+2}$  sites, *Angew. Chem. Int. Ed.* 60 (2020) 4588.
- [10] F. Chen, L.-L. Liu, J.-J. Chen, W.-W. Li, Y.-P. Chen, Y.-J. Zhang, J.-H. Wu, S.-C. Mei, Q. Yang, H.-Q. Yu, Efficient decontamination of organic pollutants under high salinity conditions by a nonradical peroxyomonosulfate activation system, *Water Res.* 191 (2021), 116799.
- [11] H. Li, C. Shan, B. Pan, Fe(III)-Doped g- $\text{C}_3\text{N}_4$  mediated peroxyomonosulfate activation for selective degradation of phenolic compounds via high-valent iron-oxo species, *Environ. Sci. Technol.* 52 (4) (2018) 2197–2205.
- [12] N. Jiang, H. Xu, L. Wang, J. Jiang, T. Zhang, Nonradical oxidation of pollutants with single-atom-Fe(III)-activated persulfate: Fe(V) being the possible intermediate oxidant, *Environ. Sci. Technol.* 54 (21) (2020) 14057–14065.
- [13] J. Lee, U. von Gunten, J.-H. Kim, Persulfate-based advanced oxidation: critical assessment of opportunities and roadblocks, *Environ. Sci. Technol.* 54 (6) (2020) 3064–3081.
- [14] F. Calle-Vallejo, D. Loffreda, M.T.M. Koper, P. Sautet, Introducing structural sensitivity into adsorption–energy scaling relations by means of coordination numbers, *Nat. Chem.* 7 (5) (2015) 403–410.
- [15] S. Zhan, H. Zhang, X. Mi, Y. Zhao, C. Hu, L. Lyu, Efficient fenton-like process for pollutant removal in electron-rich/poor reaction sites induced by surface oxygen vacancy over cobalt–zinc oxides, *Environ. Sci. Technol.* 54 (13) (2020) 8333–8343.
- [16] L. Su, P. Wang, X. Ma, J. Wang, S. Zhan, Regulating local electron density of iron single sites by introducing nitrogen vacancies for efficient photo-fenton process, *Angew. Chem. Int. Ed.* 60 (39) (2021) 21261–21266.
- [17] Y. Zong, X. Guan, J. Xu, Y. Feng, Y. Mao, L. Xu, H. Chu, D. Wu, Unraveling the overlooked involvement of high-valent cobalt-oxo species generated from the cobalt(II)-activated peroxyomonosulfate process, *Environ. Sci. Technol.* 54 (24) (2020) 16231–16239.
- [18] S. Rezgui, A. Amrane, F. Fourcade, A. Assadi, N. Adhoum, Electro-Fenton catalyzed with magnetic chitosan beads for the removal of Chlordimeform insecticide, *Appl. Catal. B Environ.* 226 (2018) 346–359.
- [19] X. Wang, Z. Chen, X. Zhao, T. Yao, W. Chen, R. You, C. Zhao, G. Wu, J. Wang, W. Huang, Regulation of coordination number over single Co sites: triggering the efficient electroreduction of  $\text{CO}_2$ , *Angew. Chem. Int. Ed.* 57 (2018) 1944–1948.
- [20] H. Shang, X. Zhou, J. Dong, A. Li, X. Zhao, Q. Liu, Y. Lin, J. Pei, Z. Li, Z. Jiang, D. Zhou, L. Zheng, Y. Wang, J. Zhou, Z. Yang, R. Cao, R. Sarangi, T. Sun, X. Yang, X. Zheng, W. Yan, Z. Zhuang, J. Li, W. Chen, D. Wang, J. Zhang, Y. Li, Engineering unsymmetrically coordinated  $\text{Cu}-\text{Si}_3\text{N}_4$  single atom sites with enhanced oxygen reduction activity, *Nat. Commun.* 11 (1) (2020) 3049.
- [21] D. Zhao, K. Sun, W. Cheong, L. Zheng, C. Zhang, S. Liu, X. Cao, K. Wu, Y. Pan, Z. Zhuang, Synergistically interactive pyridinic-N-MoP sites: identified active centers for enhanced hydrogen evolution in alkaline solution, *Angew. Chem. Int. Ed.* 59 (2020) 8982–8990.
- [22] W. Zang, A. Sumboja, Y.-Y. Ma, H. Zhang, Y. Wu, S. Wu, H. Wu, Z. Liu, C. Guan, J. Wang, S. Pennycook, Single Co atoms anchored in porous N-doped carbon for efficient zinc air battery cathodes, *ACS Catal.* 8 (2018) 8961–8969.

- [23] C. He, Y. Zhang, Y. Zhang, L. Zhao, L.-P. Yuan, J. Zhang, J. Ma, J.-S. Hu, Molecular evidence for metallic cobalt boosting CO<sub>2</sub> electroreduction on pyridinic nitrogen, *Angew. Chem. Int. Ed.* 59 (12) (2020) 4914–4919.
- [24] Chen, Z.Y.; Song; Cai; J.Y.; Zheng; X.S.; Han; D.D.; YS, Tailoring the d-Band Centers Enables Co4N Nanosheets To Be Highly Active for Hydrogen Evolution Catalysis. *Angew. Chem. Int. Ed.* 2018, 57, 5076–5080.
- [25] L. Su, P. Wang, X. Ma, J. Wang, S. Zhan, Regulating local electron density of iron single site by nitrogen vacancy for efficient photo-Fentonprocess, *Angew. Chem. Int. Ed.* 60 (39) (2021) 21261–21266.
- [26] M. Ha, D.Y. Kim, M. Umer, V. Gladkikh, C.W. Myung, K.S. Kim, Tuning metal single atoms embedded in N<sub>x</sub>C<sub>y</sub> moieties toward high-performance electrocatalysis, *Energy Environ. Sci.* 14 (6) (2021) 3455–3468.
- [27] X.-F. Li, Q.-K. Li, J. Cheng, L. Liu, Q. Yan, Y. Wu, X.-H. Zhang, Z.-Y. Wang, Q. Qiu, Y. Luo, Conversion of dinitrogen to ammonia by FeN<sub>3</sub>-embedded graphene, *J. Am. Chem. Soc.* 138 (28) (2016) 8706–8709.
- [28] L. Yu, G. Zhang, C. Liu, H. Lan, H. Liu, J. Qu, Interface stabilization of undercoordinated iron centers on manganese oxides for nature-inspired peroxide activation, *ACS Catal.* 8 (2) (2018) 1090–1096.
- [29] W.W. Rudolph, R. Mason, The hydrothermal formation of hydronium alunite from aqueous Al<sub>2</sub>(SO<sub>4</sub>)<sub>3</sub> solution and the characterization of the solid, *Z. Phys. Chem.* 216 (2002) 1061–1083.
- [30] Dong, X.; Chen, Z.; Tang, A.; Dionysiou, D.D.; Yang, H., Mineral Modulated Single Atom Catalyst for Effective Water Treatment. *Adv. Funct. Mater.*, 2111565.
- [31] X. Peng, J. Wu, Z. Zhao, X. Wang, H. Dai, Y. Wei, G. Xu, F. Hu, Activation of peroxymonosulfate by single atom Co-N-C catalysts for high-efficient removal of chloroquine phosphate via non-radical pathways: electron-transfer mechanism, *Chem. Eng. J.* 429 (2022), 132245.
- [32] X. Zhao, X. Li, Z. Zhu, W. Hu, H. Zhang, J. Xu, X. Hu, Y. Zhou, M. Xu, H. Zhang, G. Hu, Single-atom Co embedded in BCN matrix to achieve 100% conversion of peroxymonosulfate into singlet oxygen, *Appl. Catal. B* 300 (2022), 120759.
- [33] J.-G. Kim, H.-B. Kim, W.-G. Jeong, K. Baek, Enhanced-oxidation of sulfanilamide in groundwater using combination of calcium peroxide and pyrite, *J. Hazard. Mater.* 419 (2021), 126514.
- [34] L.-S. Zhang, X.-H. Jiang, Z.-A. Zhong, L. Tian, Q. Sun, Y.-T. Cui, X. Lu, J.-P. Zou, S.-L. Luo, Carbon nitride supported high-loading Fe single-atom catalyst for activation of peroxymonosulfate to generate O<sub>2</sub><sup>·</sup> with 100% selectivity, *Angew. Chem. Int. Ed.* 60 (40) (2021) 21751–21755.
- [35] B. Hxa, J.B. Ning, W.A. Da, A. Lw, C. Ysb, A. Zc, A. Jm, Z.B. Tao, Improving PMS oxidation of organic pollutants by single cobalt atom catalyst through hybrid radical and non-radical pathways, *Appl. Catal. B Environ.* 263 (2020), 118350.
- [36] B. Liu, W. Guo, W. Jia, H. Wang, S. Zheng, Q. Si, Q. Zhao, H. Luo, J. Jiang, N. Ren, Insights into the oxidation of organic contaminants by Co(II) activated peracetic acid: The overlooked role of high-valent cobalt-oxo species, *Water Res* 201 (2021), 117313.
- [37] J. Jiang, Z. Zhao, J. Gao, T. Li, M. Li, D. Zhou, S. Dong, Nitrogen vacancy-modulated peroxymonosulfate nonradical activation for organic contaminant removal via high-valent cobalt-oxo species, *Environ. Sci. Technol.* 56 (9) (2022) 5611–5619.
- [38] Y. Li, T. Yang, S. Qiu, W. Lin, J. Yan, S. Fan, Q. Zhou, Uniform N-coordinated single-atomic iron sites dispersed in porous carbon framework to activate PMS for efficient BPA degradation via high-valent iron-oxo species, *Chem. Eng. J.* 389 (2020), 124382.
- [39] X. Li, X. H. S. Xi, S. Miao, J. Ding, W. Cai, S. Liu, X. Yang, H. Yang, J. Gao, J. Wang, Y. Huang, T. Zhang, B. Liu, Single cobalt atoms anchored on porous N-doped graphene with dual reaction sites for efficient fenton-like catalysis, *J. Am. Chem. Soc.* 140 (2018) 12469–12475.
- [40] X. Liang, D. Wang, Z. Zhao, T. Li, Z. Chen, Y. Gao, C. Hu, Engineering the low-coordinated single cobalt atom to boost persulfate activation for enhanced organic pollutant oxidation, *Appl. Catal. B* 303 (2022), 120877.
- [41] J.R. Kitchin, N. Rskov, J.K. Bartea, M.A. Chen, J. G, Modification of the surface electronic and chemical properties of Pt (111) by subsurface 3d transition metals, *J. Chem. Phys.* 120 (21) (2004) 10240–10246.
- [42] G. Yang, J. Zhu, P. Yuan, Y. Hu, G. Qu, B.-A. Lu, X. Xue, H. Yin, W. Cheng, J. Cheng, W. Xu, J. Li, J. Hu, S. Mu, J.-N. Zhang, Regulating Fe-spin state by atomically dispersed Mn-N in Fe-N-C catalysts with high oxygen reduction activity, *Nat. Commun.* 12 (1) (2021) 1734.
- [43] J. Miao, Y. Zhu, J. Lang, J. Zhang, S. Cheng, B. Zhou, L. Zhang, P.J.J. Alvarez, M. Long, Spin-state-dependent peroxymonosulfate activation of single-atom M–N moieties via a radical-free pathway, *ACS Catal.* 11 (15) (2021) 9569–9577.
- [44] X. Kong, J. Ke, Z. Wang, Y. Liu, Y. Wang, W. Zhou, Z. Yang, W. Yan, Z. Geng, J. Zeng, Co-based molecular catalysts for efficient CO<sub>2</sub> reduction via regulating spin states, *Appl. Catal. B* 290 (2021), 120067.
- [45] K.-M. Zhao, S. Liu, Y.-Y. Li, X. Wei, G. Ye, W. Zhu, Y. Su, J. Wang, H. Liu, Z. He, Z.-Y. Zhou, S.-G. Sun, Insight into the mechanism of axial ligands regulating the catalytic activity of Fe–N<sub>4</sub> sites for oxygen reduction reaction, *Adv. Energy Mater.* 12 (11) (2022) 2103588.
- [46] R. Li, Y. Yue, Z. Chen, X. Chen, J. Zhao, Selective hydrogenation of acetylene over Pd–Sn catalyst: Identification of Pd<sub>2</sub>Sn intermetallic alloy and crystal plane-dependent performance, *Appl. Catal. B* 279 (2020), 119348.
- [47] Y. Wang, Z. Tong, K. Jiang, P. Da, G. Zheng, Reduced mesoporous Co<sub>3</sub>O<sub>4</sub> nanowires as efficient water oxidation electrocatalysts and supercapacitor electrodes, *Adv. Energy Mater.* 4 (16) (2014) 1400696.
- [48] N. Yao, G. Wang, H. Jia, J. Yin, H. Cong, S. Chen, W. Luo, Intermolecular energy gap-induced formation of high-valent cobalt species in CoOOH surface layer on cobalt sulfides for efficient water oxidation, *Angew. Chem. Int. Ed.* 61 (28) (2022), e202117178.